
DISSERTATION

INDEPENDENT MEASUREMENT OF THE T2K NEAR DETECTOR CONSTRAINT
USING THE OFF-AXIS PI-ZERO DETECTOR

Submitted by
Matthew Gregory Hogan
Department of Physics

In partial fulfillment of the requirements
For the Degree of Doctor of Philosophy
Colorado State University
Fort Collins, Colorado
Fall 2019

Doctoral Committee:

Advisor: Walter Toki

Robert Wilson

Norman Buchanan

Wen Zhou

Copyright by Matthew Gregory Hogan 2019
All Rights Reserved

ABSTRACT

INDEPENDENT MEASUREMENT OF THE T2K NEAR DETECTOR CONSTRAINT USING THE OFF-AXIS PI-ZERO DETECTOR

The Tokai to Kamioka (T2K) experiment is a long-baseline neutrino oscillation experiment hosted in Japan in search for electron neutrino appearance in a high purity muon neutrino beam. In order to constrain the systematic uncertainties in the oscillation analysis, a dedicated near detector (ND) complex called ND280 is located 280 meters from the neutrino production source in line of the beam. To date, the Fine Grain Detector (FGD) in ND280 has provided the ND constraint using a binned maximum likelihood estimate fit. This thesis describes the effort to validate the ND constraint using the same framework, but with an independent data set from the ND280 Pi-Zero Detector (PØD). Expanding on previously developed PØD selections, new selections have been developed to select neutrino and antineutrino events in one and multiple track topologies on water and carbon. These selections are shown to have similar sensitivity to the T2K flux and cross section systematic uncertainties. Using the same parameterization as the official ND constraint result, a hypothesis test was conducted between the PØD-only and FGD-only data fit results. A p-value of 0.2865 was obtained indicating the two data sets are likely describing the same population of neutrinos and their interactions in T2K.

ACKNOWLEDGEMENTS

I would like to first thank Elliott Forney for making a publicly accessible L^AT_EX template available at <https://github.com/idfah/csuthesis>. I also thank the T2K BANFF group and the T2K collaboration for supporting this analysis. I give thanks to my loving wife Hannah who has supported me through my graduate career. I want to acknowledge the support from my family and friends. I could not have made it this far without them.

I acknowledge the support of the United States Department of Energy under Grant Contracts DEFG0293ER40788 and DESC0017740 to support my research. I also acknowledge my advisers Robert Wilson and Walter Toki for supporting me with grant proposals and guiding me on my journey through graduate school.

Contents

ABSTRACT	ii
ACKNOWLEDGEMENTS	iii
Contents	iv
List of Tables	v
List of Figures	vi
Chapter 1 The BANFF Fit Model Parameters	1
1.1 Fit Binning	1
1.2 Penalty Terms and Systematic Uncertainties	5
1.2.1 Flux Model Parameters	5
1.2.2 Detector Inefficiencies And Bins Normalization Parameters	12
1.2.3 Cross Section Model	33
1.3 BANFF Fit Parameterization Summary	41
Bibliography	43

List of Tables

1.1	Flux Binning and Uncertainties	8
1.2	List of Detector Systematics in the Analysis	14
1.3	Eigenvalues of the Sample Covariance	32
1.4	Cross Section Model Fit Parameters in the BANFF Fit	40

List of Figures

1.1	Main Track Momentum Resolution for the ν_μ in FHC Mode CC 1-Track Sample	3
1.2	Main Track Angular Residuals for the ν_μ in FHC Mode CC 1-Track Sample . .	4
1.3	The BANFF Prefit Flux Covariance Matrix	6
1.4	Neutrino Flux Prediction at SK and Flux Bin Edges	7
1.5	Vertex Distribution Showing Evidence of PØD Bulging	16
1.6	Bin Normalizations Edges for the ν_μ in FHC Mode Samples	25
1.7	Bin Normalization Edges for the $\bar{\nu}_\mu$ in RHC Mode Samples	26
1.8	Bin Normalizations for the ν_μ Background in RHC Mode Samples	27
1.9	Event Variations in Observable Normalization Bins	28
1.10	Detector Penalty Covariance Matrix	30
1.11	Principal Component for the Sample Variance	32
1.12	Cross Section Parameters Prefit Covariance and Correlation Matrices	39

Chapter 1

The BANFF Fit Model Parameters

In addition to the likelihood ratio maximization, the BANFF fit includes three sources of systematic uncertainties: neutrino flux, cross section model, and detector inefficiencies. This chapter explores the fit binning and penalty terms in the test statistic used for this analysis. The sources of systematic uncertainty, also referred to just as systematics, will be defined and their effect on the analysis.

This chapter is presented in the following order. The first section explores the method to define fit bins in the likelihood ratio. The second section is divided into three subsections to define the parameterization of each penalty term in the test statistic. The penalty terms, discussed in order, are the neutrino flux model, the detector inefficiencies, and lastly the cross section model. These three terms directly affect the flux of neutrinos, efficiency of reconstruction, and the cross section for ν_α terms, respectively, in the predicted rate equation given in (??).

1.1 Fit Binning

The PØD-only BANFF fit uses the samples described in Chapter ?? to evaluate the log-likelihood ratio term, χ_{LLR}^2 . Since this is a binned likelihood in $(p, \cos \theta)$, the bin edges need to be defined first.

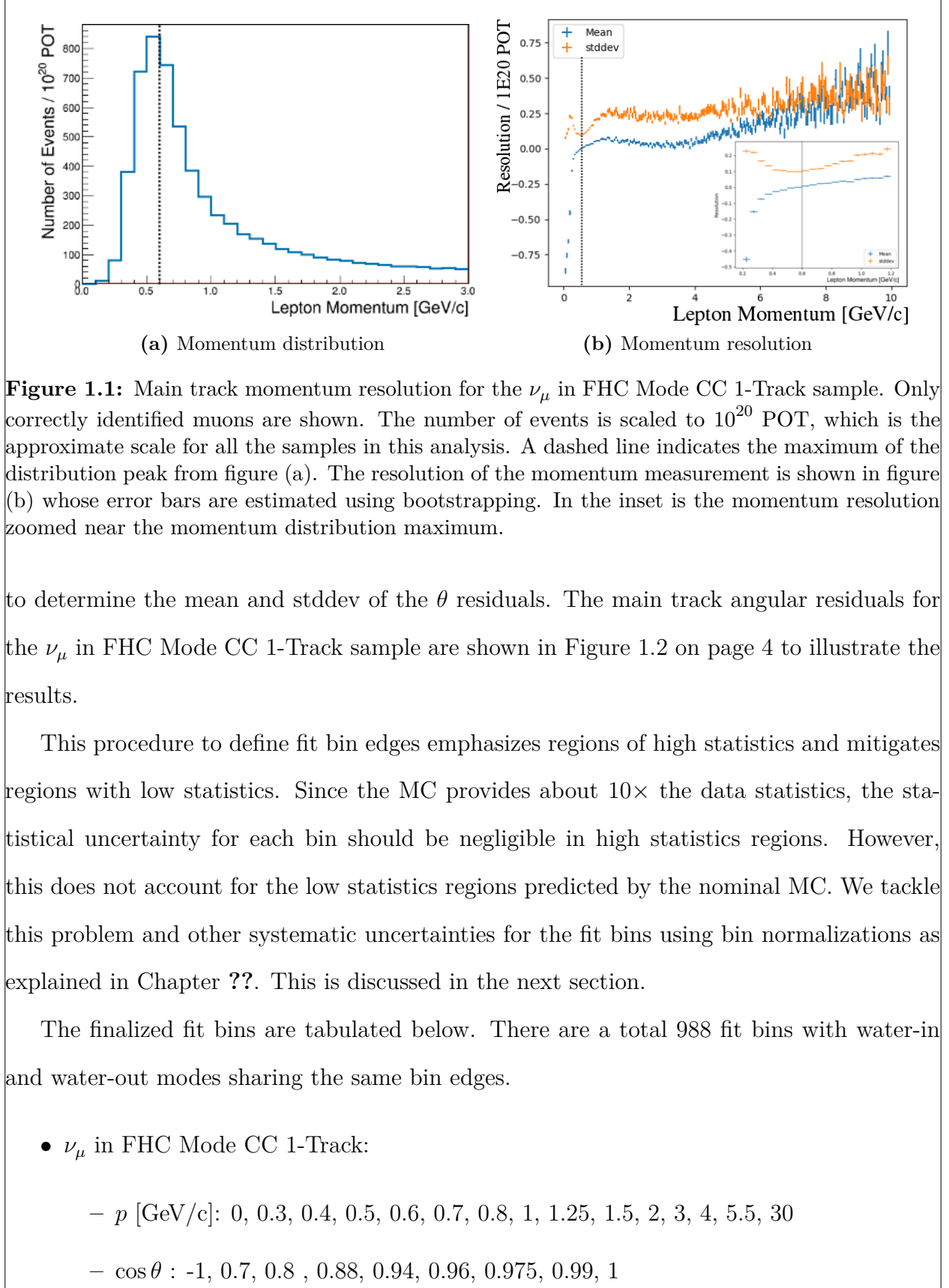
The BANFF fit binning is optimized to ensure at least 1 predicted Monte Carlo (MC) event in each bin for every PØD sample when scaled to the collected data POT. The fit bins must also account for detector smearing effects. In order to mitigate smearing and event migration, the reconstructed kinematics were examined to their MC truth value using only correctly identified leptons in one-dimensional kinematic slices. The kinematics are scanned across their full phase spaces in order to understand the required width for a fit bin. The first fit bin is always defined starting from the kinematic maximum.

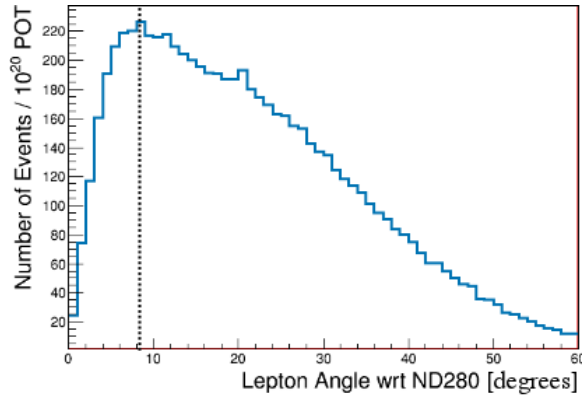
To determine the optimal momentum fit bins, the momentum resolution with the MC truth matched muon is analyzed. The momentum resolution is defined as

$$R(r, t) = \frac{r - t}{t},$$

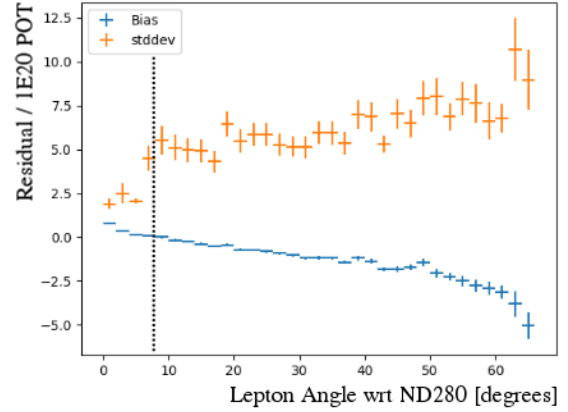
where r is the reconstructed momentum and t is the true muon momentum. The mean (bias) and standard deviation (stddev) of R are used as proxies for the true bias and resolution for the prediction. Both quantities and prediction errors were extracted using a bootstrapping algorithm [19] in very fine bins of reconstructed momentum. The bootstrapping algorithm works by random sampling with replacement of the true muon momentum. For each bias and stddev prediction, at least 1000 bootstrapping samples were generated. Each bootstrap bias and stddev value were saved to calculate a prediction mean and error. In the case of relatively “large” prediction errors, additional 10000 bootstrapping samples were generated. The main track momentum resolution for the ν_μ in FHC Mode CC 1-Track sample is shown in Figure 1.1 on page 3 to illustrate the results.

The optimal $\cos\theta$ fit bins were determined in a very similar manner with the momentum fit bins. While the fit bins and physics are dictated in $\cos\theta$ space, the detector smearing is a function θ . In addition, since the angle can be nearly zero for the most forward-going tracks, the resolution was not used to characterize the angular uncertainties. Instead, the difference (“residual”) between the true and reconstructed angle θ with respect to (wrt) the ND280 Z-axis were analyzed. The same bootstrapping algorithm described above was used





(a) Angular distribution



(b) Angular residuals

Figure 1.2: Main track angular residuals for the ν_μ in FHC Mode CC 1-Track sample. Only correctly identified muons are shown. The number of events is scaled to 10^{20} POT, which is the approximate scale for all the samples in this analysis. A dashed line indicates the maximum of the distribution peak from figure (a). The residual of the angular measurement is shown in figure (b) whose error bars are estimated using bootstrapping.

- ν_μ in FHC Mode CC N-Tracks:
 - p [GeV/c]: 0, 0.4, 0.5, 0.6, 0.7, 0.8, 1, 1.2, 1.5, 1.8, 2.2, 2.7, 3.5, 5, 10, 30
 - $\cos \theta$: -1, 0.65, 0.77, 0.85, 0.9, 0.94, 0.97, 0.99, 1
- $\bar{\nu}_\mu$ in RHC Mode CC 1-Track:
 - p [GeV/c]: 0, 0.4, 0.5, 0.6, 0.7, 0.8, 1, 1.25, 1.5, 2, 3, 30
 - $\cos \theta$: -1, 0.82, 0.87, 0.9, 0.93, 0.95, 0.97, 0.99, 1
- $\bar{\nu}_\mu$ in RHC Mode CC N-Tracks:
 - p [GeV/c]: 0, 0.5, 0.9, 1.25, 1.6, 2, 3, 8, 30
 - $\cos \theta$: -1, 0.8, 0.89, 0.95, 0.97, 0.99, 1
- ν_μ in RHC CC 1-Track:
 - p [GeV/c]: 0, 0.4, 0.6, 0.8, 1.1, 2, 10
 - $\cos \theta$: -1, 0.78, 0.84, 0.89, 0.92, 0.95, 0.97, 0.98, 0.99, 1

- ν_μ in RHC CC N-Tracks:

- p [GeV/c]: 0, 0.4, 0.6, 0.8, 1, 1.5, 2, 3, 10

- $\cos \theta$: -1, 0.7, 0.8, 0.85, 0.9, 0.94, 0.965, 0.98, 0.99, 1

1.2 Penalty Terms and Systematic Uncertainties

This section expands on the penalty terms, and hence fit parameters, in the BANFF fit. The cross section and flux penalty terms in this analysis are identical to the previous near detector constraint studies [8, 32]. This provides a one-to-one comparison between the PØD-only and FGD-only flux and cross section predictions. However, due to the different detector technologies between the PØD and FGD, different bin normalization parameters are necessary.

The first set of fit parameters described are the flux terms. This is followed by a description of the fit bin normalization parameters. The final topic is a description of the cross section parameters.

1.2.1 Flux Model Parameters

The T2K neutrino flux model is a description of the neutrino beam spectrum for each run period and flavor. This model includes simulations of the proton beam interactions and subsequent hadron production at the target. The predicted hadron production rate, including inside and outside the graphite target, is tuned to the results from the replica target¹ experiment NA61/SHINE [5] and other hadron production experiments. The uncertainties in the unoscillated flux tuning are dominated by hadron production. Smaller effects on the unoscillated flux uncertainty include the proton beam profile, off-axis angle, horn current,

¹The NA61/SHINE experiment has two graphite targets. A thin 2 cm target and a thick 90 cm target. The thick target is a replica of the T2K graphite target.

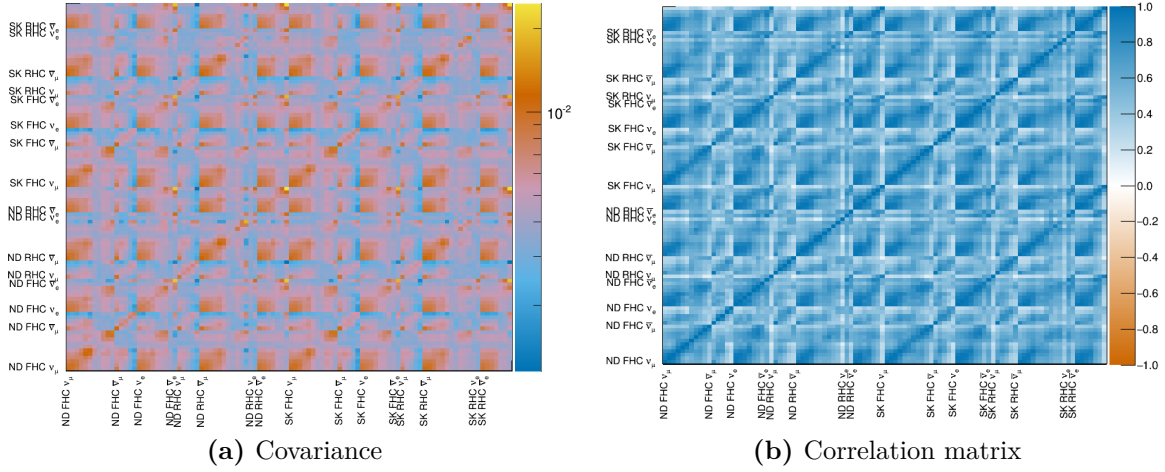


Figure 1.3: The BANFF prefit flux covariance matrix. Figure (a) shows the covariance matrix which is the uncertainty of the normalization for the neutrino flux at both ND280 and SK. The covariance matrix is divided into submatrices in groups by detector, beam mode, and neutrino flavor. Figure (b) is the linear correlation coefficient for each covariance term.

and horn alignment. Further details about the flux model and uncertainties can be found in the following reference [2].

The flux penalty term in the BANFF fit is defined, as previously seen in Chapter ??, as

$$\chi_{\text{Flux}}^2 = (\vec{b} - \vec{b}_0)^T (V_b^{-1}) (\vec{b} - \vec{b}_0). \quad (1.1)$$

As a remainder, all penalty terms in this analysis have the form of (1.1). Each flux parameter, b_i , is a neutrino energy bin normalization starting at one (1). Each parameter is defined as

$$b_i = \frac{N'_{\nu_\alpha, i}}{N_{\nu_\alpha, i}}, \quad (1.2)$$

where $N_{\nu, i}$ and $N'_{\nu, i}$ are the predicted and ND constrained ν_α event rates, respectively, in the i th energy bin. In other words, *each flux term is a ratio of rates. Further, all penalty terms and covariance terms are dimensionless.* The flux bins are differentiated by neutrino energy, horn current/polarity (FHC mode and RHC mode), neutrino flavor (ν_μ , $\bar{\nu}_\mu$, ν_e , and $\bar{\nu}_e$), and detector (ND280 and SK). The flux binning and covariance matrix, shown in Figure 1.3 on

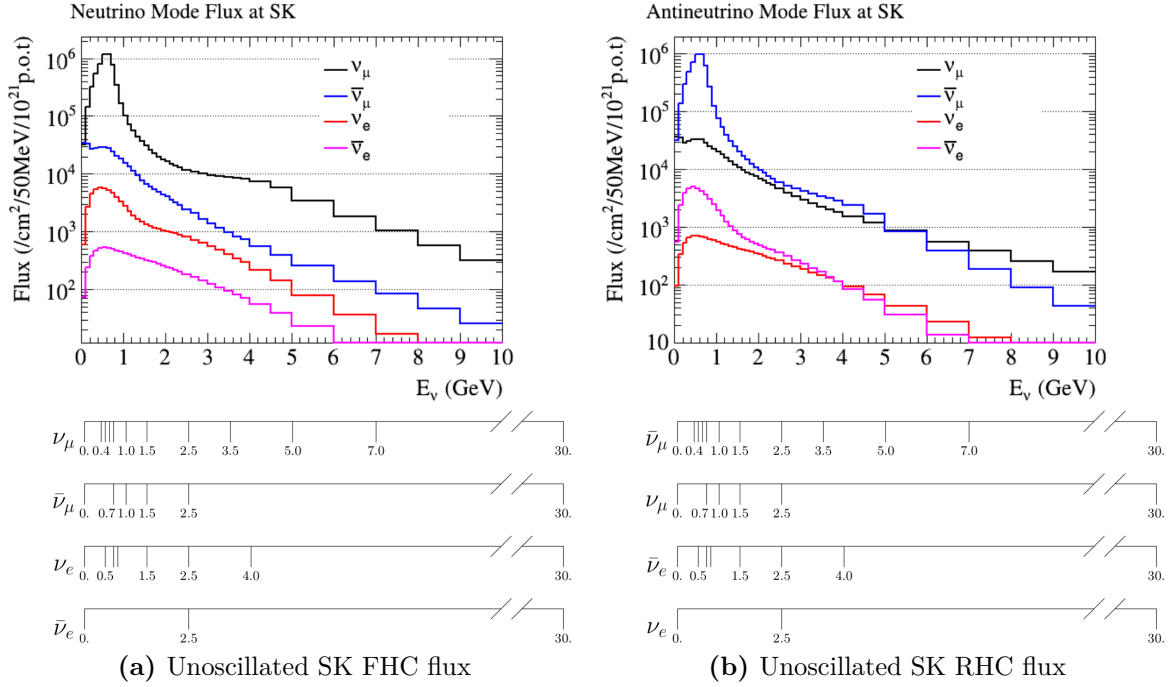


Figure 1.4: Neutrino Flux Prediction at SK and Flux Bin Edges. The flux prediction for FHC (RHC) mode is shown in figure on the left (right). The flux normalization parameters have an assigned energy range and are the same for both the SK and ND280 detectors. The energy binning used is shown below the plots.

page 6, is provided by the T2K flux group. Also shown in Figure 1.3 on page 6 is the Pearson linear correlation coefficient matrix which is defined as

$$\rho_{i,j} = \frac{V_{i,j}}{\sqrt{V_{i,i}V_{j,j}}}, \quad (1.3)$$

where V is the covariance matrix and i and j are bins in V .

There are 50 ND280 and 50 SK flux parameters to yield a total of 100 flux normalizations. In addition, the bin edges are shared between the ND280 and SK. The SK neutrino flux and the flux bin edges are shown in Figure 1.4 on page 7. In the BANFF fit, both ND280 and SK flux parameters are extracted simultaneously. This is achieved using correlations between ND280 and SK flux parameters as shown in Figure 1.3 on page 6. The tabulated flux parameters/bins in this analysis are given in Table 1.1 on page 8. Each flux bin is assigned an initial value of one (1) for all events in that neutrino energy bin. A postfit value

of 1.1 indicates that all events in that energy bin have an additional weight of 1.1, signaling that the postfit prefers to increase that neutrino flux by 10%. Equivalently, this means N'_ν is 10% greater than N_ν .

Table 1.1: Flux binning and uncertainties used in the BANFF fit.

Fit index	Beam mode	Bin edges [GeV]	Prefit
0	ND280 ν_μ FHC	0.0 - 0.4	1 ± 0.100909
1		0.4 - 0.5	1 ± 0.099431
2		0.5 - 0.6	1 ± 0.092025
3		0.6 - 0.7	1 ± 0.085239
4		0.7 - 1.0	1 ± 0.105356
5		1.0 - 1.5	1 ± 0.104375
6		1.5 - 2.5	1 ± 0.073612
7		2.5 - 3.5	1 ± 0.068993
8		3.5 - 5.0	1 ± 0.082334
9		5.0 - 7.0	1 ± 0.097308
10		7.0 - 30	1 ± 0.114706
11	ND280 $\bar{\nu}_\mu$ FHC	0.0 - 0.7	1 ± 0.103804
12		0.7 - 1.0	1 ± 0.084158
13		1.0 - 1.5	1 ± 0.081349
14		1.5 - 2.5	1 ± 0.085208
15		2.5 - 30	1 ± 0.087735
16	ND280 ν_e FHC	0.0 - 0.5	1 ± 0.091336
17		0.5 - 0.7	1 ± 0.089699
18		0.7 - 0.8	1 ± 0.084648
19		0.8 - 1.5	1 ± 0.079722
20		1.5 - 2.5	1 ± 0.079766

Fit index	Beam mode	Bin edges [GeV]	Prefit
21	ND280 $\bar{\nu}_e$ FHC	2.5 - 4.0	1 ± 0.081399
22		4.0 - 30	1 ± 0.095795
23		0.0 - 2.5	1 ± 0.072069
24		2.5 - 30	1 ± 0.142921
25	ND280 ν_μ RHC	0.0 - 0.7	1 ± 0.094066
26		0.7 - 1.0	1 ± 0.079866
27		1.0 - 1.5	1 ± 0.080948
28		1.5 - 2.5	1 ± 0.083251
29	ND280 $\bar{\nu}_\mu$ RHC	2.5 - 30	1 ± 0.082653
30		0.0 - 0.4	1 ± 0.107277
31		0.4 - 0.5	1 ± 0.098851
32		0.5 - 0.6	1 ± 0.089710
33		0.6 - 0.7	1 ± 0.084692
34		0.7 - 1.0	1 ± 0.106871
35		1.0 - 1.5	1 ± 0.098711
36		1.5 - 2.5	1 ± 0.073350
37		2.5 - 3.5	1 ± 0.070520
38		3.5 - 5.0	1 ± 0.092905
39		5.0 - 7.0	1 ± 0.089083
40		7.0 - 30	1 ± 0.134911
41	ND280 ν_e RHC	0.0 - 2.5	1 ± 0.066214
42		2.5 - 30	1 ± 0.086977
43	ND280 $\bar{\nu}_e$ RHC	0.0 - 0.5	1 ± 0.095575
44		0.5 - 0.7	1 ± 0.089033
45		0.7 - 0.8	1 ± 0.088406

Fit index	Beam mode	Bin edges [GeV]	Prefit
46	SK ν_μ FHC	0.8 - 1.5	1 ± 0.081472
47		1.5 - 2.5	1 ± 0.078353
48		2.5 - 4.0	1 ± 0.089427
49		4.0 - 30	1 ± 0.156972
50		0.0 - 0.4	1 ± 0.102555
51		0.4 - 0.5	1 ± 0.101771
52		0.5 - 0.6	1 ± 0.092573
53		0.6 - 0.7	1 ± 0.084265
54		0.7 - 1.0	1 ± 0.102271
55		1.0 - 1.5	1 ± 0.084528
56		1.5 - 2.5	1 ± 0.066909
57		2.5 - 3.5	1 ± 0.072355
58		3.5 - 5.0	1 ± 0.085299
59		5.0 - 7.0	1 ± 0.096725
60		7.0 - 30	1 ± 0.114112
61	SK $\bar{\nu}_\mu$ FHC	0.0 - 0.7	1 ± 0.103129
62		0.7 - 1.0	1 ± 0.078327
63		1.0 - 1.5	1 ± 0.082367
64		1.5 - 2.5	1 ± 0.082121
65		2.5 - 30	1 ± 0.085123
66	SK ν_e FHC	0.0 - 0.5	1 ± 0.090918
67		0.5 - 0.7	1 ± 0.087065
68		0.7 - 0.8	1 ± 0.082527
69		0.8 - 1.5	1 ± 0.076514
70		1.5 - 2.5	1 ± 0.075773

Fit index	Beam mode	Bin edges [GeV]	Prefit
71	SK $\bar{\nu}_e$ FHC	2.5 - 4.0	1 ± 0.082078
72		4.0 - 30	1 ± 0.092882
73		0.0 - 2.5	1 ± 0.071921
74		2.5 - 30	1 ± 0.128982
75	SK ν_μ RHC	0.0 - 0.7	1 ± 0.093954
76		0.7 - 1.0	1 ± 0.076369
77		1.0 - 1.5	1 ± 0.074900
78		1.5 - 2.5	1 ± 0.078108
79	SK $\bar{\nu}_\mu$ RHC	2.5 - 30	1 ± 0.077505
80		0.0 - 0.4	1 ± 0.108593
81		0.4 - 0.5	1 ± 0.101912
82		0.5 - 0.6	1 ± 0.092787
83		0.6 - 0.7	1 ± 0.082669
84		0.7 - 1.0	1 ± 0.102090
85		1.0 - 1.5	1 ± 0.087732
86		1.5 - 2.5	1 ± 0.068117
87		2.5 - 3.5	1 ± 0.069902
88		3.5 - 5.0	1 ± 0.091711
89		5.0 - 7.0	1 ± 0.084736
90		7.0 - 30	1 ± 0.115488
91	SK ν_e RHC	0.0 - 2.5	1 ± 0.066204
92		2.5 - 30	1 ± 0.082645
93	SK $\bar{\nu}_e$ RHC	0.0 - 0.5	1 ± 0.095453
94		0.5 - 0.7	1 ± 0.088889
95		0.7 - 0.8	1 ± 0.085644

Fit index	Beam mode	Bin edges [GeV]	Prefit
96		0.8 - 1.5	1 ± 0.078536
97		1.5 - 2.5	1 ± 0.075246
98		2.5 - 4.0	1 ± 0.086384
99		4.0 - 30	1 ± 0.152507

1.2.2 Detector Inefficiencies And Bins Normalization Parameters

In the BANFF fit, bin normalization parameters are used to evaluate the detector inefficiency penalty term, χ_{Det}^2 . Varying fit bins without constraint is nonphysical due to known detector inefficiencies and their systematic uncertainties. Since improperly modeled inefficiencies can cause events to migrate from bin-to-bin, numerous fake “toy experiments” are performed to evaluate the systematic uncertainties in detector inefficiencies. When all toy experiments are analyzed together, correlated variations among fit bins become apparent. These correlations provide the constraints on freely changing bin normalizations. We will see the result of running such toy experiment variations in the coming pages. Hitherto in this thesis, detector inefficiency uncertainties will be referred to as detector systematics.

All the detector systematics are evaluated either as observable variations or weights. An observable variation affects the physical observables of selected events like the calculated energy loss of a track in the PØD. A weight is a multiplicative factor that alters the normalization of a single event in a bin. There are detector systematics that affect the PØD-only, TPC-only, or both.

This section is organized as follows. The systematic uncertainties relevant to this analysis are described in Section 1.2.2.1. The systematics treatment model for the detector systematics developed to evaluate their effects on the analysis is described in Section 1.2.2.2. The

detector systematics penalty term used in the BANFF fit is described in Section 1.2.2.3. Finally, the procedure to determine the initial bin normalization is presented in Section 1.2.2.4.

1.2.2.1 Detector Systematics

The BANFF fit analysis has the ability to evaluate the effect of detector systematic uncertainties on the analysis samples. Since this analysis uses the PØD and TPC detectors, systematics that affect both must be included. There are two types of systematic treatments in the BANFF analysis: observable variations and weights. Each treatment relies on the method of throwing a random number to evaluate the systematic's impact on the sample observables. Efficiency-like systematics are treated as weights to the MC predictions in order to evaluate the uncertainty the systematic has on an analysis. Observable variation systematics are evaluated as shifts to physically measured quantities like momentum and track length. Both rely on data-driven studies by comparing data and MC predictions in a control sample.

The complete set of detector systematics and their treatment in the analysis are listed in Table 1.2 on page 14. The TPC-only systematics have been used in previous BANFF fit analysis are included in this analysis. Details on the TPC-only systematics are discussed in the following references [2, 32]. There are four PØD-only detector systematics that are considered for this BANFF fit analysis:

- The PØD detector energy loss scale,
- The PØD detector energy loss resolution,
- The PØD-TPC inter-detector matching efficiency, and
- The PØD detector fiducial mass.

All of the PØD-only systematics were initially analyzed in the PØD ν_μ CC-0 π cross section analysis [3]. The PØD-only systematics are discussed further below.

Systematic effect	Affected Detector	Treatment
TPC cluster eff.	TPC	efficiency
TPC tracking eff.	TPC	efficiency
TPC charge misassignment	TPC	efficiency
TPC momentum resol.	TPC	observable variation
TPC momentum scale	TPC	observable variation
B field distortion	TPC	observable variation
Pion secondary interactions	All	efficiency
Proton secondary interactions	All	efficiency
TPC Particle ID	TPC	observable variation
TPC track quality eff.	TPC	efficiency
PØD energy loss scale	PØD	observable variation
PØD energy loss resol.	PØD	observable variation
PØD mass	PØD	(see text)
PØD-TPC matching eff.	PØD+TPC	(see text)

Table 1.2: List of detector systematics in the analysis. The systematics listed above the horizontal line are discussed in the following reference [2]. The PØD mass and track matching systematics were not available in the BANFF framework and treated as uncorrelated additions to the total covariance matrix.

The PØD energy loss scale and resolution affect the measured momentum in the PØD and are very significant sources of uncertainty. In the ν_μ CC-0 π cross section analysis, the same selection as the ν_μ in FHC Mode CC 1-Track selection, the scale and resolution contributed 1.3% and 6.7%, respectively, to the cross section uncertainty. Those large uncertainties can be attributed to the design of the PØD. It is optimized for π^0 detection as opposed to a dedicated tracking detector like the FGD. Slight variations in the track reconstruction can significantly alter the energy loss as measured in (??).

The remaining systematics, the PØD mass and the PØD-TPC matching efficiency, were not available to analyze in toy experiments variations. They were not implemented in the BANFF framework and unavailable to implement due to time constraints on this author. Instead, they were treated as additional uncorrelated systematics on each bin normalization uncertainty with the normalization value remaining fixed. The treatment of these two systematics will be discussed shortly.

The PØD mass uncertainty is a normalization systematic which affects the event rate. This is a challenging systematic for analyses of recent T2K data due to increasingly faulty sensors to measure the water content. The procedure to fill the water bags required filling them in unison to prevent uneven bulging. However, faulty sensors would provide poor quality data, hence bags were under and overfilled. This effect alters the expected event rate as a function of position.

Another problem with the mass uncertainty is due to structure deformations in the PØD. To understand how the PØD has deformed, it is important to understand how the PØD is mounted in the ND280 detector. Each corner of the PØD is mounted to the ND280 basket leaving the those corners spatially fixed. When the water bags are filled, the WT volume expanded or “bulged” from the middle filling small air gaps. The upstream end of the PØD, the Upstream ECal, resisted deformations since it is physically against the ND280 support structure. However, the Central ECal (CECal) has no such restriction since there is a $\mathcal{O}(1)$ cm gap between it and the TPC. The CECal, which has a design thickness of 304 mm, was observed to bulge about 7-8 mm from its center as well [31].

This left more water volume, and importantly more mass, in the most downstream water bags compared to the upstream bags. This additional mass or bulging effect is evident in the vertex distribution as a function of the Z-position as shown in Figure 1.5 on page 16.

Prior PØD analyses have estimated the mass uncertainty using similar toy experiment techniques, but did not integrate them into the BANFF framework. In particular in the ν_μ in CC-0 π analysis [3], the PØD mass had an 1.5% systematic effect on the cross section. Since the PØD mass uncertainty estimate was determined using the same toy experiment variation method, a conservative estimate of 2% on the mass uncertainty is included in this analysis.

The PØD and TPC (PØD-TPC) matching efficiency is estimated to have a small systematic effect on the analysis. It was analyzed to have over a 99.8% data and MC efficiency in the single track ν_μ CC-0 π analysis and thus was neglected. However, since this analysis

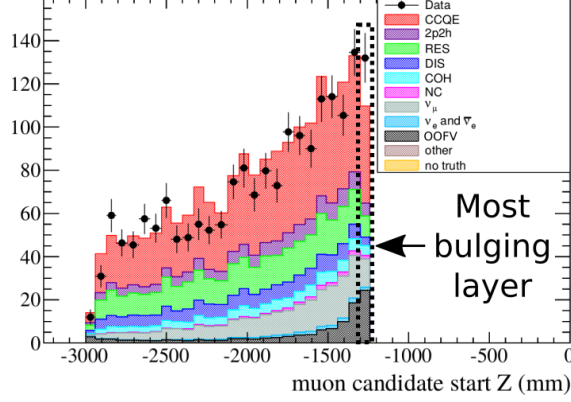


Figure 1.5: Vertex distribution showing evidence of bulging. In the $\bar{\nu}_\mu/\nu_\mu$ cross section ratio analysis, a significant excess of events in the most downstream layer of the PØD (black, dashed line box) was observed. Initially thought to be OOFV events, the analyzers removed the most downstream and upstream layers in their analysis. This distribution was produced using the run 5, RHC period using selection precuts 1 through 4 and a having a positive track in the TPC. Each event is categorized by true interaction mode according to NEUT. This figure was altered for clarity from the following reference [10].

includes > 1 track samples, the matching efficiency for non-single track samples is unknown. The best constraint is from the private T2K technical note on the single bin $\bar{\nu}_\mu/\nu_\mu$ cross section analysis [10], which estimated the uncertainty at less than 0.14% using a in-house matching algorithm. Since this analysis uses a different track matching algorithm, the uncertainty is not guaranteed to remain constant across $(p, \cos\theta)$ bins. A conservative estimate of 1% for the PØD-TPC matching efficiency was chosen in order to account for the inherent uncertainty in this systematic.

Now that we know the systematics that affect the analysis, we can now begin to understand how the detector systematic penalty term χ_{Det}^2 is modeled in the BANFF fit.

1.2.2.2 Systematic Treatment Models

As mentioned above, there are two types of systematic treatments: efficiency-like correction weights and observable variations. This section will discuss both treatments and the model extrapolation methods to evaluate their effects on all BANFF fit samples. First is a description of efficiency-like systematic corrections and then followed by a description of the observable variation methods.

Efficiency-like corrections alter the number of predicted events as measured by a control sample² (CS). The model used to evaluate efficiency-like systematics is given by

$$\epsilon_{\text{Data}}(o) = \left(\frac{\epsilon_{\text{Data}}(o)}{\epsilon_{\text{MC}}(o)} \right)_{\text{CS}} \epsilon_{\text{MC}}(o), \quad (1.4)$$

where $\epsilon_{\text{MC}}/\epsilon_{\text{Data}}$ denotes the mean selection efficiency of the MC/data as a function of some observable kinematic o , and $()_{\text{CS}}$ refers to the efficiency measured in the CS. We need to update this model to account for statistical uncertainties in the CS. The updated model, with o dependence assumed, is now

$$\epsilon'_{\text{Data}} = \left(\frac{\epsilon_{\text{Data}} + x_{\text{Data}} \cdot \sigma_{\epsilon_{\text{Data}}}}{\epsilon_{\text{MC}} + x_{\text{MC}} \cdot \sigma_{\epsilon_{\text{MC}}}} \right)_{\text{CS}} \epsilon_{\text{MC}} \quad (1.5)$$

where $\sigma_{\epsilon_{\text{MC}}}/\sigma_{\epsilon_{\text{Data}}}$ is the standard deviation of the efficiency of the MC/Data and x_{Data} and x_{MC} are uncorrelated, random normally distributed numbers from $\mathcal{N}(\mu = 0, \sigma^2 = 1)$. All the variations are applied to the event, simultaneously affecting all observables, and the event selection is rerun. A weight is derived depending if the event is selected, w_{eff} , or not selected, w_{ineff} . These weights are given below

$$\begin{aligned} w_{\text{eff}} &= \frac{\epsilon'_{\text{Data}}}{\epsilon_{\text{MC}}} \\ w_{\text{ineff}} &= \frac{1 - \epsilon'_{\text{Data}}}{1 - \epsilon_{\text{MC}}}. \end{aligned} \quad (1.6)$$

Observable variation systematics are evaluated as shifts to physically measured quantities like particle track momentum and track length. The systematic can be evaluated in two different ways:

1. If the reconstructed observable, o_{reco} , has a known true value, o_{true} , then the difference between those two is used as scaling. The varied observable is given by

²Each control sample is validated in T2K prior to introduction to the BANFF analysis.

$$o' = o_{\text{true}} + (o_{\text{reco}} - o_{\text{true}})(s + x\sigma_s), \quad (1.7)$$

where s is the mean scaling parameter used to match the true value, σ_s is the uncertainty on s , and x is a random number from $\mathcal{N}(\mu = 0, \sigma^2 = 1)$. The mean scaling parameter and its uncertainty are determined from the standard deviations observed in the data and MC by

$$s = \frac{\delta^{\text{data}}}{\delta^{\text{MC}}} \quad \sigma_s = s \left| \frac{\sigma_{\delta^{\text{data}}}}{\delta^{\text{data}}} - \frac{\sigma_{\delta^{\text{MC}}}}{\delta^{\text{MC}}} \right|. \quad (1.8)$$

2. If the MC reconstructed observable is corrected to match the mean from some CS reconstructed observable. The varied observable in this case is given by

$$o' = o_{\text{Nom}} + \Delta o + x\sigma_{\Delta o}, \quad (1.9)$$

where o' is the varied observable value, o_{Nom} is the nominal MC value, Δo is the average correction to the observable, $\sigma_{\Delta o}$ is the uncertainty on the correction, and x is a random, normal number from $\mathcal{N}(\mu = 0, \sigma^2 = 1)$.

Additional uncertainties from the magnetic field are also special cases of the 2nd observable variation method specifically for the TPC momentum [32]. They are:

- The TPC laser calibration corrections are applied after the magnetic field (B-field) mapping corrections. The B-field corrections are applied at event reconstruction while the calibration corrections are treated as a systematic uncertainty. The varied momentum is given by

$$p' = p_{\text{Nom}} + x(p_{\text{Map}} - p_{\text{Nom}}), \quad (1.10)$$

where p_{Nom} is the nominal MC prediction using the B-field corrections and p_{Map} is the updated momentum using the additional laser calibration mapping.

- The momentum depends on some scale parameter s . The varied momentum due to the scale uncertainty is given by

$$p' = p_{\text{Nom}} (1 + x\sigma_s), \quad (1.11)$$

where σ_s is the uncertainty on the scale. In this parameterization, s is the scale of the magnet current.

After all observables are varied and applied to the event, the event selections are applied again. By applying the selection cuts after all variations, the full impact of the systematic on the sample and analysis bins can be evaluated.

1.2.2.3 Detector Systematics Penalty

The bin normalization penalty parameters are restrictions on freely varying fit bins. To determine the correlations between bins, many toy experiments are performed. As described in Section 1.2.2.2, each toy experiment varies event observables, i.e. the momentum and angle of the main track, and number of events in a fit bin. The bin normalization parameter for the i th bin, or d_i , is defined as

$$d_i = \frac{\langle N_i \rangle_{\text{toys}}}{N_i}, \quad (1.12)$$

where N_i predicted number of events in fit bin i and $\langle N_i \rangle_{\text{toys}}$ is the average number of events in fit bin i evaluated over all toy experiments (toys). The predicted event rate for bin i is given by

$$N_i = \sum_k^{N_{\text{MC}}} \delta_{i,k}^{\text{bin}} w_k, \quad (1.13)$$

where N_{MC} being the number of unweighted MC events, $\delta_{i,k}^{\text{bin}}$ determines if the k th event goes into analysis bin i as a function of $(p, \cos \theta)$, and w_k is the product of all of the weights applied to the k th event. The weights used in (1.13) are

$$w_k = w_k^{\text{POT}} \times w_k^{\text{Flux}} \times w_k^{\text{xsec}} \times w_k^{\text{Det}}, \quad (1.14)$$

(see (??) for all possible weights). The number of events in fit bin i , averaged over all toy experiments (toys), is given by

$$\begin{aligned}\langle N_i \rangle_{\text{toys}} &= \frac{1}{N_{\text{toys}}} \sum_{t=1}^{N_{\text{toys}}} (N_i)_t \\ &= \frac{1}{N_{\text{toys}}} \sum_{t=1}^{N_{\text{toys}}} \left(\sum_k^{N_{\text{MC}}} [\delta_{i,k}^{\text{bin}} w_k] \right)_t,\end{aligned}\tag{1.15}$$

where now each MC event has a toy variation out of N_{toys} total toys. We average the results of the toys to smooth out variations among all toy experiments. In this analysis, and in previous BANFF analyses as well, $N_{\text{toys}} = 2000$ toys were generated as to have a small sample size uncertainty.

As stated before, all the penalty parameters are dimensionless and the detector systematics covariance matrix must be constructed carefully. The bin-to-bin event rate covariance, $V_{i,j}^{\text{Cov}}$, between bins i and j is

$$V_{i,j}^{\text{Cov}} = \frac{1}{N_{\text{toys}}} \sum_{t=1}^{N_{\text{toys}}} \left((N_i)_t - \langle N_i \rangle_{\text{toys}} \right) \left((N_j)_t - \langle N_j \rangle_{\text{toys}} \right),\tag{1.16}$$

where $(N_i)_t$ is defined in (1.15). We also need to account for statistical uncertainties in the fit bins, and so let us define $V_{i,j}^{\text{Stat}}$ as

$$V_{i,j}^{\text{Stat}} = \delta_{i,j} \sum_k^{N_{\text{MC}}} \delta_{i,k}^{\text{bin}} w_k^2,\tag{1.17}$$

where $\delta_{i,j}$ is the Kronecker delta function. In order to incorporate $V_{i,j}^{\text{Cov}}$ and $V_{i,j}^{\text{Stat}}$ uncertainties, the total detector covariance matrix, $V_{i,j}^{\text{Det}}$, in the BANFF fit is defined as

$$V_{i,j}^{\text{Det}} = \frac{(V_{i,j}^{\text{Cov}} + V_{i,j}^{\text{Stat}})}{N_i N_j},\tag{1.18}$$

which is indeed dimensionless since we divided out the predicted event rate in bins i and j .

As stated before, the PØD mass and track matching efficiency systematics are treated as uncorrelated systematics in the analysis. In order to propagate their systematic uncertainties into the analysis, the detector covariance matrix given in (1.18) needs to be updated. The updated covariance matrix is given by

$$V_{i,j}^{\text{Det}} \leftarrow \left(\tilde{V}_{i,j}^{\text{Det}} + \tilde{\sigma}_{\text{Mass}}^2 + \tilde{\sigma}_{\text{Match}}^2 \right) d_i d_j, \quad (1.19)$$

where $\tilde{V}_{i,j}^{\text{Det}}$ is the fractional covariance

$$\tilde{V}_{i,j}^{\text{Det}} = \frac{V_{i,j}^{\text{Det}}}{d_i d_j}, \quad (1.20)$$

d_i/d_j are the bin normalization parameters, and $\tilde{\sigma}_{\text{Mass}}^2 = 2\%$ and $\tilde{\sigma}_{\text{Match}}^2 = 1\%$ are the PØD mass and PØD-TPC matching efficiency systematic uncertainties, respectively, estimated in Section 1.2.2.1. Together, the two additional sources of uncertainty increase each term in the covariance matrix by $0.0005 d_i d_j$. Specifically, the uncertainty in all the bin normalization parameters (square-root of the diagonal terms in the covariance matrix) increases by about 2.23%. The updated detector covariance matrix now accounts for the PØD mass and TPC matching inefficiency systematics.

The penalty term, χ_{Det}^2 , in the fit is given by

$$\chi_{\text{Det}}^2 = \left(\vec{d} - \vec{d}_0 \right)^T \left(V^{\text{Det}} \right)^{-1} \left(\vec{d} - \vec{d}_0 \right)^T, \quad (1.21)$$

where \vec{d}_0 is the initial set values of the parameters and V^{Det} is given by (1.19).

1.2.2.4 Bin Normalization Parameters

While there could be one observable normalization for each analysis bin, a single normalization can be assigned to multiple analysis bins. The purpose is to reduce the number of fit parameters since the time to fit increases non-linearly with the number of fit parameters

and events. Previously, the observable normalization edges were determined by combining fit bins with “similar” covariance. This method proved problematic since the fit bins with relatively higher statistics were shared with the same observable normalization parameter. This left the remaining low statistics regions of $(p, \cos \theta)$ phase space more susceptible to systematic variations in the toy experiments.

A new procedure was developed to improve the shortcomings of old procedure which required careful consideration of the statistical uncertainties and variations between observable normalization prefit values. This procedure can be imagined as reducing the number of contours in a topographic map while considering external constraints from other sensing data. The first step in the procedure is to initialize all of the observable normalization bin edges to be the same as the fit bin edges. All steps after this are performed iteratively.

Starting with observable normalization bin with the highest statistics, a decision is made to merge it with all immediate adjacent bins. If the individual fractional errors differ significantly before the merge, do not merge them. In this analysis, a factor of 10 in fractional uncertainty was determined to sufficiently describe bin similarity by using values larger and smaller than 10 and observing no significant differences in the end result. Additionally if the two unmerged bin normalizations differ by more than 10%, perform the bin merging. This step serves to smooth out the observable normalization prefit space. The procedure is also written in pseudocode in Algorithm 1.

The results of the procedure are shown visually in Figure 1.6 on page 25, Figure 1.7 on page 26, and Figure 1.8 on page 27. While the problem of a few fit bins, each having large statistics, assigned to a single observable normalization parameter is still present, fluctuations between adjacent observable normalization parameters is iteratively minimized. A considerable drawback to designing bin normalizations in this way of varying detector systematics in toy experiments is that not all detector systematics affect the fit observables $(p, \cos \theta)$ in the same way. There are non-symmetric systematics and they are especially non-Gaussian in their effects. Therefore, the covariance matrix from (1.18) is not an exact representation of

```

repeat
  redo  $\leftarrow$  False;
  for each normalization bin  $d$  do //sorted from min to max  $\delta\%$ 
    for each neighboring analysis bin  $f$  do
       $d' \leftarrow$  normalization bin assigned to  $f$ ;
      if  $d'$  is same as  $d$  then
        Continue to next analysis bin;
      end
      if  $\delta\%(d) \geq 10 \times \delta\%(d')$  then
         $d$  is assigned as normalization bin for  $f$ ;
        redo  $\leftarrow$  True;
        Continue to next analysis bin;
      end
      max_norm  $\leftarrow$  max(norm( $d$ ), norm( $d'$ ));
      min_norm  $\leftarrow$  min(norm( $d$ ), norm( $d'$ ));
      if max_norm  $\geq 1.1 \times$  min_norm then
         $d$  is assigned as normalization bin for  $f$ ;
        redo  $\leftarrow$  True;
      end
    end
  end
  Recalculate bin normalizations;
until redo is False;

```

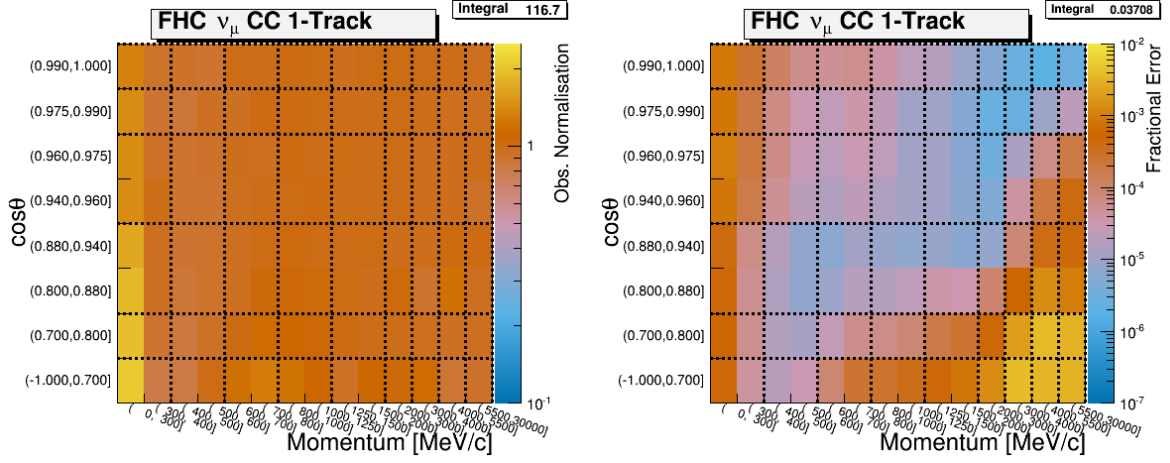
Algorithm 1: Algorithm to merge normalization bins. The “ $\delta\%$ ” operator returns the fractional statistical uncertainty for the bin. Since multiple fit bins can be assigned to a single normalization bin, the statistics of all fits bins are included. The “norm” operator returns the normalization value for a normalization bin determined by (1.13). Finally, the min/max functions return the minimum/maximum element in a tuple, respectively.

the detector systematics. To demonstrate this, results of varied number of events are shown in Figure 1.9 on page 28. However, the bin normalization standard deviations are very wide and able to effectively cover the range of possible bin normalizations, which minimizes the non-Gaussian effects of the systematic. All the varied toy experiment results are provided in Appendix ??.

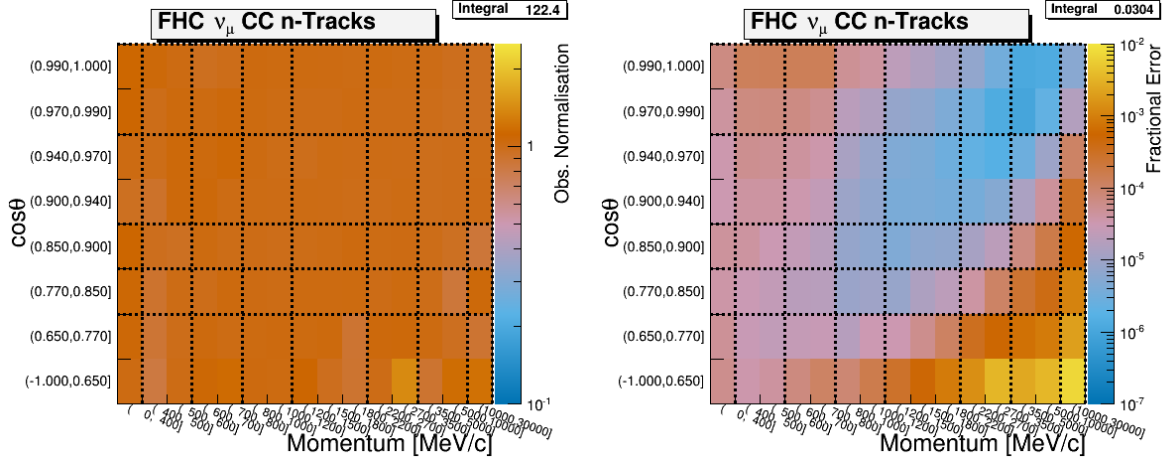
The detector systematic that had the largest effect on the observable normalization prediction was the PØD energy loss resolution (ELossRes) which alters the amount of particle energy deposited in the PØD. This systematic was developed for the ν_μ CC-0 π cross section analysis, it was identified as the largest detector systematic uncertainty in the cross section measurement [33]. When the deposited energy in the PØD is varied using (1.7), it also changes the distance the truth matched particle travels in the PØD. Hence, this systematic changes the likelihood of a particle being reconstructed as a track. The observed effect is that for bins with relatively low muon momentum, the number of predicted events can vary in a non-Gaussian manner as shown in Figure 1.9 on page 28.

An unexpected phenomenon was observed when comparing the toy experiments with and without the ELossRes variation applied. With the ELossRes variation disabled in the toy experiments, a relatively large shift in the bin prediction was observed compared to the nominal prediction. This shift was expected, but was not expected was the direction of the shift as shown in Figure 1.9 on page 28. In most cases, the shift is below the nominal MC value. However, in many of the bins, that the shape location of the prediction is above the expectation. This behavior was unexpected prior to running the toy experiment variations.

A relationship between the prediction shape location and selection purity as a function of $(p, \cos \theta)$ was discovered. In high purity $(p, \cos \theta)$ -regions of the 1-Track samples, the shape location of the prediction in the disabled ELossRes toy experiments was below the nominal MC prediction. When the 1-Track sample purity was lower, however, the shape location was above it. This effect is likely due to events migrating from the 1-Track samples into the N-Tracks samples due to multiple particles in the event.

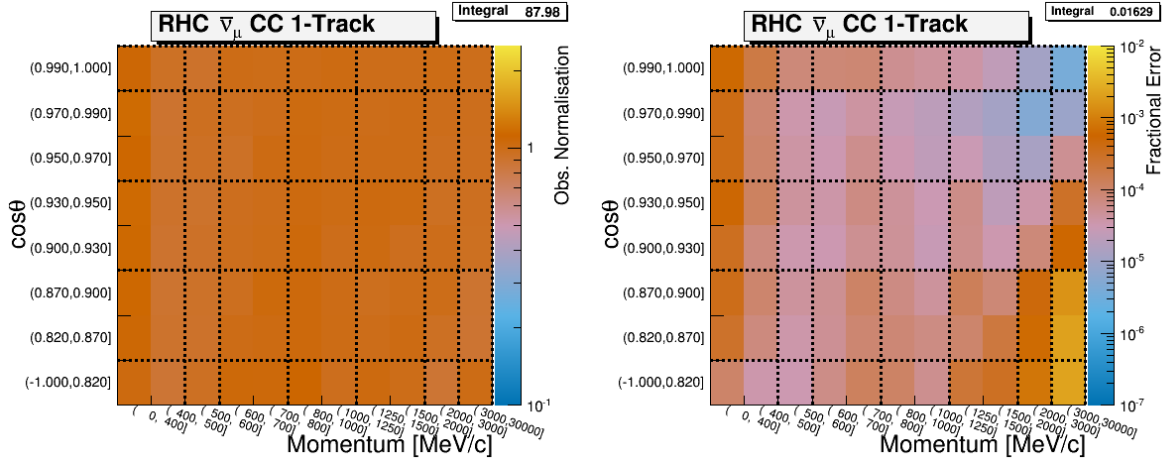


(a) The ν_μ in FHC Mode CC 1-Track sample

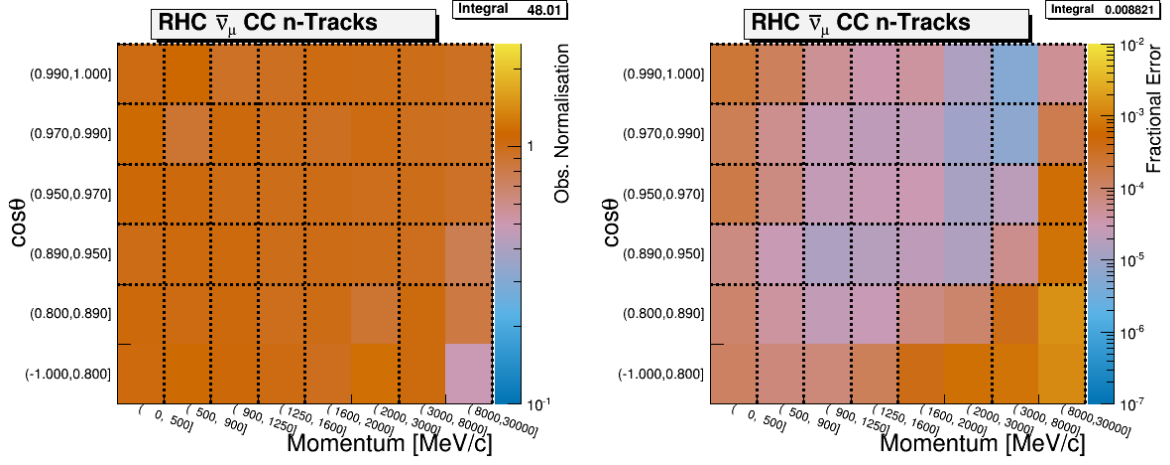


(b) The ν_μ in FHC Mode CC N-Tracks sample

Figure 1.6: Bin normalization edges for the ν_μ in FHC Mode samples. The left and right plots show the bin normalization and the bin statistical fractional error, respectively, if each fit bin had a single bin normalization. The dashed lines indicate the edges of the bin normalization parameters finalized for this analysis. Water-in and water-out modes are qualitatively the same.

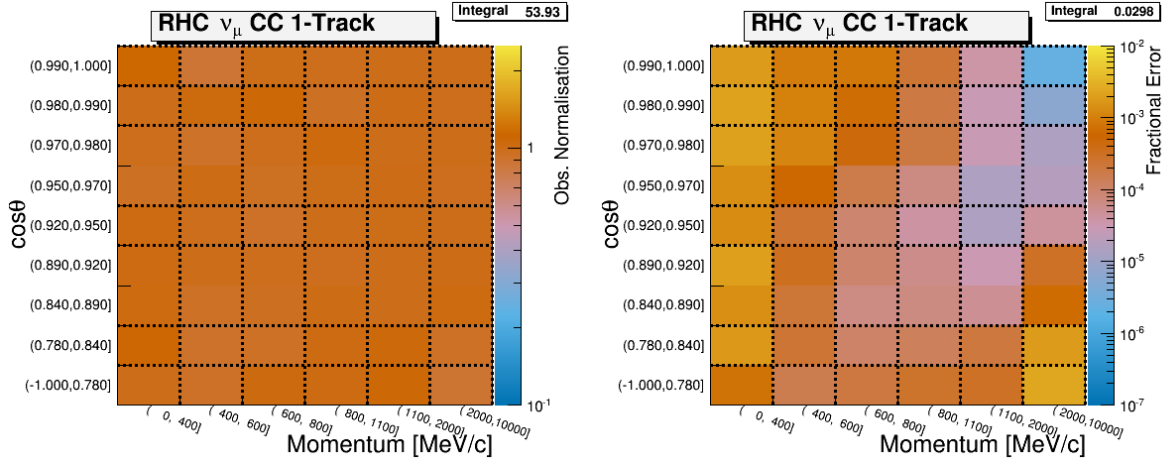


(a) The $\bar{\nu}_\mu$ in RHC Mode CC 1-Track sample

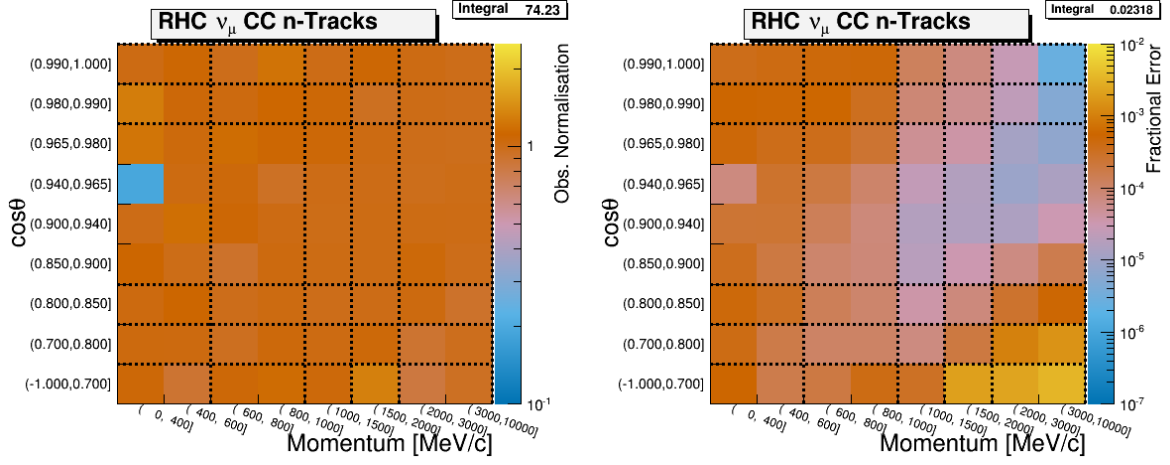


(b) The $\bar{\nu}_\mu$ in RHC Mode CC N-Tracks sample

Figure 1.7: Bin normalization edges for the $\bar{\nu}_\mu$ in RHC Mode samples. There are two plots shown for each sub-figure. The left and right plots show the bin normalization and the bin statistical fractional error, respectively, if each fit bin had a single bin normalization. The dashed lines indicate the edges of the bin normalization parameters finalized for this analysis. Water-in and water-out modes are qualitatively the same.



(a) The ν_μ in RHC CC 1-Track sample



(b) The ν_μ in RHC CC N-Tracks sample

Figure 1.8: Bin normalization edges for the ν_μ Background in RHC Mode samples. There are two plots shown for each sub-figure. The left and right plots show the bin normalization and the bin statistical fractional error, respectively, if each fit bin had a single bin normalization. The dashed lines indicate the edges of the bin normalization parameters finalized for this analysis. Water-in and water-out modes are qualitatively the same.

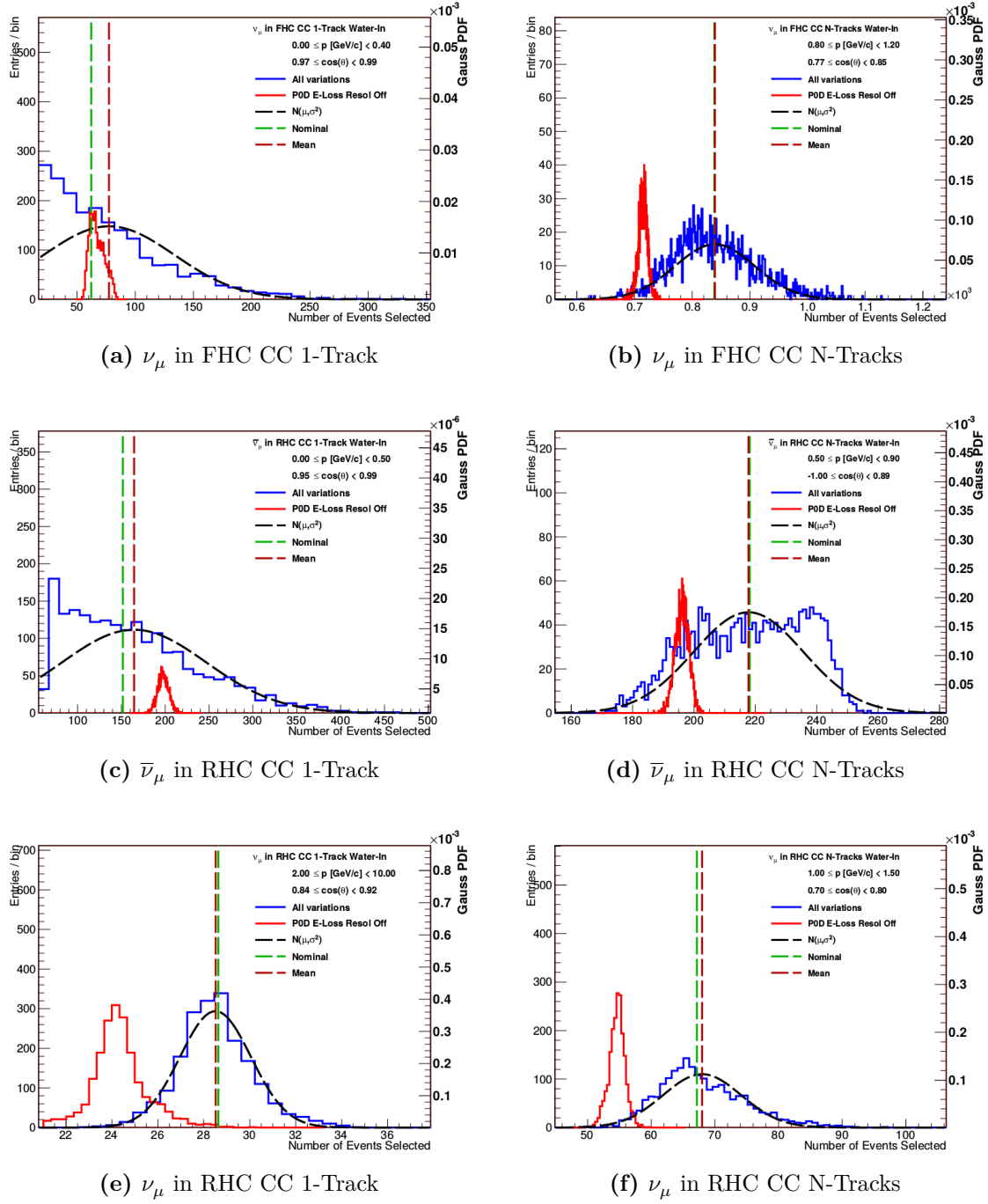


Figure 1.9: Event variations in representative observable normalization bins. Shown in each subfigure the varied event rate from all toy experiments in a particular observable normalization bin. The blue curve has all the systematics enabled while the red curve has the ELossRes systematic disabled. Vertical dashed lines show the unvaried, weighted MC prediction and varied mean of all toy experiments. The ratio of the horizontal positions of each vertical line is the profit normalization value for that bin. A Gaussian with variance extracted from the covariance matrix is shown to illustrate the bin's estimate on the normalization uncertainty.

The finalized observable normalization bins are listed below. There are in total $N_d = 461$ bin normalization parameters. The covariance matrix used in the BANFF fit is shown in Figure 1.10 on page 30. Their respective fit index, prefit value, and prefit standard deviation are tabulated in Appendix ??.

- ν_μ in FHC CC 1-Track bin normalization edges:
 - p [GeV/c]: 0, 0.4, 0.6, 0.8, 1.25, 2, 3, 4, 5.5, 30
 - $\cos\theta$: -1, 0.7, 0.8, 0.94, 0.975, 0.99, 1
- ν_μ in FHC CC N-Tracks bin normalization edges:
 - p [GeV/c]: 0, 0.4, 0.6, 0.8, 1.2, 2.2, 3.5, 10, 30
 - $\cos\theta$: -1, 0.77, 0.85, 0.9, 0.97, 1
- $\bar{\nu}_\mu$ in RHC CC 1-Track bin normalization edges:
 - p [GeV/c]: 0, 0.5, 0.6, 0.8, 1.25, 2, 3, 30
 - $\cos\theta$: -1, 0.82, 0.9, 0.95, 0.99, 1
- $\bar{\nu}_\mu$ in RHC CC N-Tracks bin normalization edges:
 - p [GeV/c]: 0, 0.5, 0.9, 1.25, 1.6, 3, 30
 - $\cos\theta$: -1, 0.89, 0.95, 0.97, 0.99, 1
- ν_μ in RHC CC T-track bin normalization edges:
 - p [GeV/c]: 0, 0.4, 0.6, 0.8, 1.1, 2, 10
 - $\cos\theta$: -1, 0.78, 0.84, 0.92, 0.95, 0.98, 0.99, 1
- ν_μ in RHC CC N-Tracks bin normalization edges:
 - p [GeV/c]: 0, 0.6, 1, 1.5, 2, 10

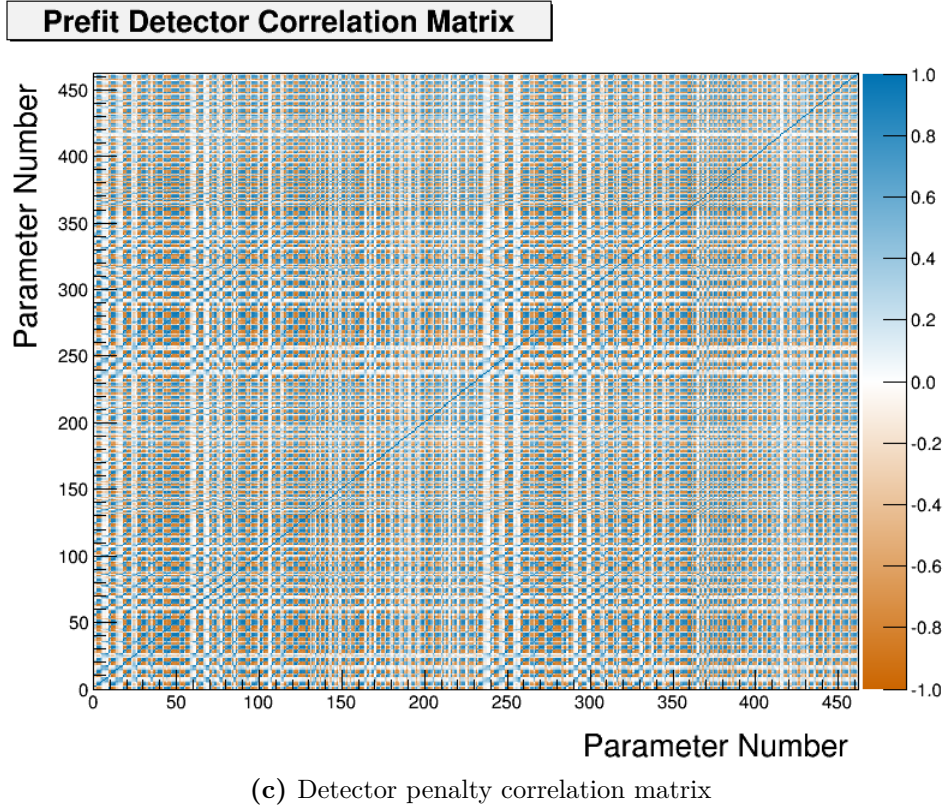
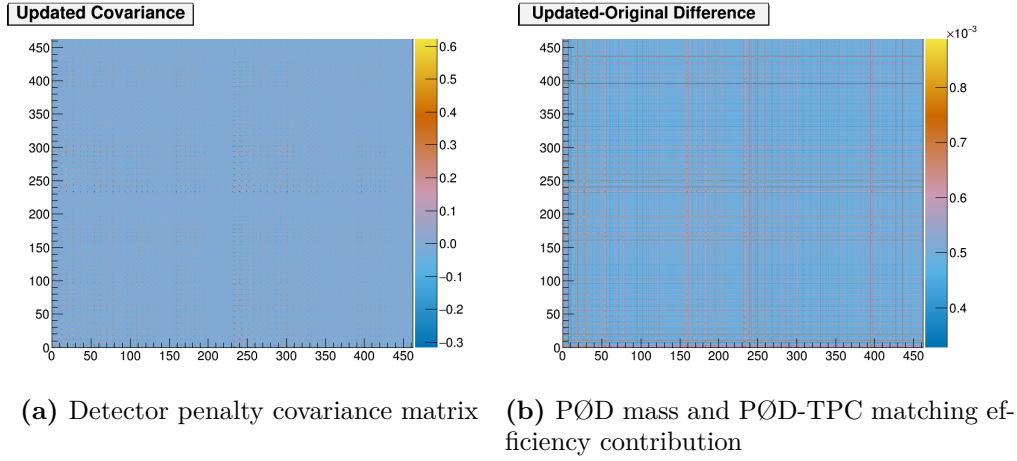


Figure 1.10: Detector penalty covariance matrix. Shown in figure (a) is covariance matrix, (b) is the is contribution from the PØD mass and PØD-TPC matching efficiency ad-hoc contributions, and (c) is the correlation matrix calculated from (a). Note that the parameter indices, which represent the bin normalization indices, are offset from their fit indices value by 99.

– $\cos \theta$: -1, 0.7, 0.8, 0.85, 0.98, 0.99, 1

To estimate how the bin normalizations may respond in the BANFF fit, principal component analysis was performed on all the toy experiments. Principal component analysis allows one to understand the amount of variance in the data. The procedure is identical to performing the eigenvalue decomposition of a square matrix M such that M is decomposed as

$$M = O^T D O,$$

where O is a orthogonal matrix of the eigenvectors, and D is a diagonal matrix of the eigenvalues. The principal components of M are the eigenvectors and their relative importance is set by the magnitude of the associated eigenvalue.

Using this prescription, we can analyze the sample variance of the toy experiments. The sample variance, S , is defined as

$$S = \frac{1}{N_{\text{toys}}} X^T X,$$

where X is a $N_{\text{toys}} \times N_d$ matrix of the predicted number of events (not the normalization!) in each normalization bin. The eigenvalue decomposition of S is given by

$$S = U^T V' U,$$

where U is the eigenvector matrix of S and V' is a diagonal matrix of the sample covariance eigenvalues sorted from largest to smallest magnitude. The sample variance eigenvalues are shown in Table 1.3 on page 32. The first, and hence largest, eigenvalue is two orders of magnitude larger than the next largest eigenvalue, which means that the majority of the bin-to-bin variance can be explained by the first eigenvector. The first eigenvector coefficients is shown in Figure 1.11 on page 32. We see that all the components are negative and centered around a central value. This result is interpreted to mean we can expect the

Index	0	1	2	3	...	458	459	460	461
Eigenvalue	2029	16.45	12.87	11.10	...	0.05325	0.05129	0.04955	0.03992

Table 1.3: Eigenvalues of the sample covariance. The values are sorted from largest to smallest in magnitude. Note that the parameter indices, which represent the bin normalization indices, are offset from their fit indices value by 99.

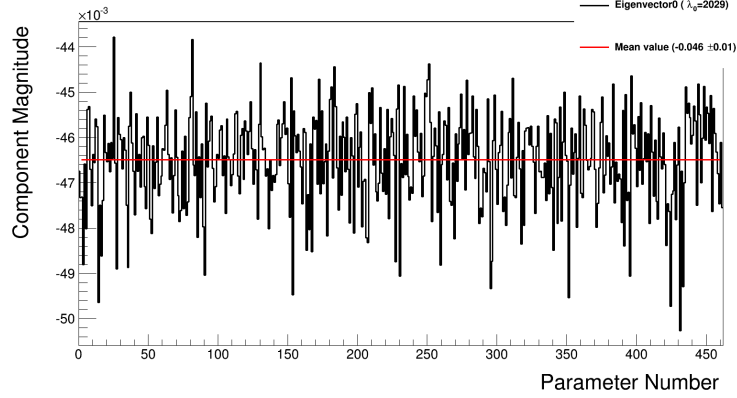


Figure 1.11: Principal component for the sample variance. This is the eigenvector associated with the largest eigenvalue of magnitude 2029. Each parameter coefficient refers to the slope of the axis that describes most of the variance in the sample. The coefficients are all negative and are of similar magnitude. Together, they suggest all the normalization parameters respond linearly and uniformly. Note that the parameter indices, which represent the bin normalization indices, are offset from their fit indices value by 99.

bins normalizations postfit values to shift all together uniformly and most likely smaller in magnitude than their prefit values.

Additionally, we can estimate the effective degrees of freedom for the bin normalization parameters. The effective degrees of freedom is given by

$$\text{df}(\lambda) = \sum_{i=0}^{N_d} \frac{v_i}{v_i + \lambda}, \quad (1.22)$$

where v_i are the eigenvalues of V' and λ is a tunable parameter [19]. The idea behind (1.22) is that although all N_d coefficients will be non-zero, they are restricted to vary by the magnitude of λ . In particular, λ represents the regularization strength for the detector systematics penalty, which is set to one ($\lambda = 1$) in the BANFF fit. If there was no (regularization) penalty, or $\lambda = 0$, then the number of degrees of freedom is $\text{df}(0)=N_d$. It is found that there

are about 137 effective degrees of freedom for the bin normalization parameters, or 29% of $N_d (= 462)$. This suggests that a much smaller number bin normalization parameters can be used in the BANFF fit analysis, and that they can have similar response to the sample variance. This is particularly important since this improves computational performance while maintaining predictability power in the ND constraint measurement. No further reduction in the number of bin normalization parameters were pursued due to time constraints.

1.2.3 Cross Section Model

There are a number of neutrino-nucleus interaction model parameters implemented in BANFF to account for the uncertainties in cross section measurements. They are frequently updated to account for new models and constraints from external data. The cross section models used in this analysis use the T2K 2017 parameterization, which is a canonical set of parameters shared among all analyses in T2K. A gross description of the cross section model is provided here with a full description in the following reference [4].

There are three types of cross section parameters: shape, normalization, and functional. A cross section shape parameter is defined as a fractional shift in the location of a certain feature in some parameter space. As a design choice, the shape location parameters all start with a prefit value of zero (0). A cross section normalization parameter, x_i^{Norm} , is defined as

$$x_i^{\text{Norm}} = \frac{p'}{p}, \quad (1.23)$$

where p and p' are NEUT nominal and ND constrained parameters, respectively. The prefit values for the normalizations are set to (1) unless specified. And finally functional parameters are scalars to model a cross section of a true kinematic. For example, if a cross section is linear in Q^2 and is given by $\sigma(Q^2) = AQ^2 + B$, A and B are the functional parameters in the model.

The next sections deal with the model parameterizations and systematic uncertainties in the NEUT version 5.3.3 [32] interaction library which is used in T2K MC and oscillation analysis.

1.2.3.1 The CCQE and CC-0 π Models

The cross section models with the largest impact on T2K’s oscillation sensitivity are CCQE and CCQE-like interactions, collectively called CC-0 π . At energies near the ν_e appearance maximum, $E_\nu = 0.6$ GeV, the CCQE interaction is the largest contributor to the neutrino cross section as shown in Figure ?? on page ???. The nominal CCQE model in NEUT is a Spectral Function (SF) from Benhar et al [6]. An alternative CCQE model incorporates the Llewellyn-Smith dipole axial form factor³ [11, 21] and BBBA05 vector form factors coupled to a Smith-Miniz Relativistic Fermi Gas [9, 24, 30] (RFG). A CCQE-like excitation mode involves correlated nucleon pair scattering called “2 particle, 2 hole” [22] (2p2h). An additional nuclear model called the “Random Phase Approximation” (RPA) [12] is used to to modify single nucleon scattering by accounting for nucleon correlations inside the nucleus [23]. The default CC-0 π model for T2K analyses is the combination of the Llewellyn-Smith+RFG model, 2p2h excitation, and RPA nuclear model. This combination was selected due to poor data matching with the SF model [32].

The selected CCQE model has three free parameters: the dipole axial form factor mass M_A^{QE} from the Llewellyn-Smith model, and two Fermi momentum parameters p_F , one for ^{12}C and one for ^{16}O that describe the momentum of nucleons on the surface of a RFG. In the past, using these parameters has been shown to work as effective parameters in T2K when unconstrained. In this analysis, these three parameter are unconstrained. In other words, a flat prior is used for M_A^{QE} , p_F^C , and p_F^O .

³A form factor is a measure of scattering amplitude in the form of the Fourier transform of some charge distribution.

For the 2p2h excitation, there are a total of 5 parameters to describe the model. Three are three normalization terms: ν interaction on ^{12}C , $\bar{\nu}$ interaction on ^{12}C , and scaling for $^{12}\text{C} \rightarrow ^{16}\text{O}$. The remaining two systematic parameters in the 2p2h model are shape parameters, one for ^{12}C and one for ^{16}O . They are used constrain the interplay of the contributing modes in 2p2h. One contributing mode is the Meson Exchange Current (MEC) which involves a virtual meson exchange between the nucleons. The other mode is nucleon-nucleon (NN) correlations which involves virtual particle exchange. A shape value of -1 determines 2p2h is completely due to MEC, 0 is the nominal MC 2p2h model, and +1 determines 2p2h is completely due to NN. Any differences in the event rate in the region between ± 1 is absorbed by a interference term. However, since no existing T2K nor external neutrino data can constrain the neutrino-induced 2p2h interaction, a flat prior is set for all 2p2h parameters.

The other nuclear interaction in the CC-0 π model uses the Nieves RPA model [23] to describe nucleon correlations. The RPA model primarily alters the single nucleon cross section and has dependence on both E_ν and Q^2 . A functional weighting scheme only in Q^2 was found to work well to mimic the inherent uncertainties in the Nieves RPA model. The functional is given by

$$w(Q^2) = \begin{cases} A\beta_0^3(x) + B\beta_1^3(x) + p_1\beta_2^3(x) + D\beta_3^3(x) & Q^2 \leq U \\ 1 + p_2 \exp(-E[Q^2 - U]), & Q^2 > U \end{cases} \quad (1.24)$$

where $x = Q^2/U$, $\beta_i^n(x)$ are the Bernstein polynomials [13]

$$\beta_i^n(x) = \binom{n}{i} x^i (1-x)^{n-i} \quad x \in [0, 1], \quad (1.25)$$

p_1 and p_2 absorb the continuity conditions,

$$p_1 = D + \frac{UE(D-1)}{3}, \quad p_2 = D - 1, \quad (1.26)$$

and A , B , D , E , and U are the functional parameters. This functional form serve to correct for collective nuclear effects not modeled in NEUT and is called the Bernstein RPA (BeRPA) model. The parameters A , B , D , and E are allowed to vary while U is fixed to prevent unwieldy correlations from appearing.

1.2.3.2 The CC-1 π Model

Another important exclusive channel in NEUT is resonance states that produce a single pion or CC-1 π . The CC-1 π model incorporates the Rein-Seghal model of neutrino-induced Δ resonance decay [15–17, 26] with lepton mass corrections [7, 18]. There are just three tunable parameters in the model. They are resonant axial mass M_A^{Res} , the axial form factor normalization C_A^5 , and the isospin=1/2 background. These three parameters are known to effectively describe neutrino-induced single pion production data from Brookhaven National Laboratory [20] and Argonne National Laboratory [25]. It is important to know that M_A^{Res} and C_A^5 are strongly anticorrelated due to the parameterization of the form factor

$$f(Q^2) = C_A^5 \left(1 + \frac{Q^2}{(M_A^{\text{Res}} c^2)^2} \right)^{-2}. \quad (1.27)$$

1.2.3.3 Coherent Pion Production

Coherent scattering refers to scattering where the wavelength of the incoming particle is larger than the target. In the case of coherent neutrino-nucleus scattering, the neutrino's wavelength given by

$$\lambda = \frac{hc}{E_\nu}$$

is larger than the size of the nucleus. In the scattering, no quantum numbers are exchanged, but the nucleus experiences a momentum boost. In coherent pion production, the in-flight virtual boson is converted into a pion with that pion exchanging a Pomeron [1] with the nucleus. The coherent scattering model is described by Rein-Sehgal [27]. Lookup tables are

used to scale the cross section to external data [32] and the Berger-Sehgal model [7]. Three tunable normalization parameters are used describe the coherent production model: CC on ^{12}C , CC on ^{16}O , and NC on all nuclei.

1.2.3.4 The CC DIS Model

The CC DIS process, which also includes multiple pion production, is modeled as a shape parameter as a function of E_ν . The parameter is has a simple uncertainty relation of

$$\frac{0.4}{E_\nu [\text{GeV}]}(\%)$$

where the uncertainty at 4.0 GeV is 10% [32].

1.2.3.5 The NC Other Model

There is one free normalization parameter for the NC processes. The NC other parameter contains the normalization uncertainties in NC DIS, single kaon production, single η -meson production, and elastic processes with a 30% fractional uncertainty [32].

1.2.3.6 Final State Interactions (FSI)

Final state interactions [14] are effects that alter final state pions from neutrino-nucleus events before the pion exits the nucleus. The microscopic model in NEUT is a cascade implementation of the Salcedo-Oset model [29] which describes interactions in the nucleus as probabilities of position and momentum. The systematics are parameterized as scattering probabilities for different interaction processes tuned to world data [28]. These processes are divided into six classes with one parameter for each. These classes are the low energy inelastic scattering (INEL), high energy INEL, pion absorption (ABS), pion production (PROD), low energy charge exchange (CEX), and high energy CEX. The low and high energy transition for both the inelastic scattering and charge exchange processes occurs at $p_\pi = 500 \text{ MeV}/c$.

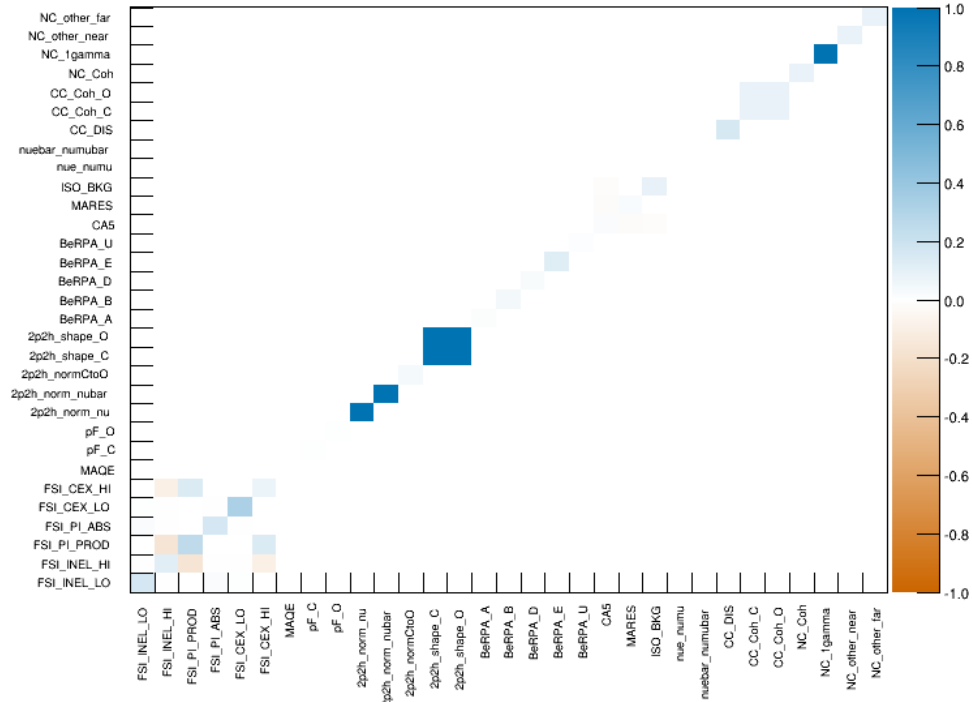
1.2.3.7 Other Fixed Parameters

As mentioned in the CC-0 π model, the BeRPA U parameter is fixed to minimize correlations with the other BeRPA scale parameters. However, there are four fixed normalization parameters in the BANFF fit since they correspond to SK only parameters. They are included in the fit in order to maintain consistency between the ND280 constraint and oscillation analysis parameterizations. In other words, they are spectators in the BANFF fit. These parameters are the CC ν_e/ν_μ event rate ratio, CC $\bar{\nu}_e/\bar{\nu}_\mu$ event rate ratio, NC 1γ event rate, and NC other far detector event rate.

1.2.3.8 Fit Parameters

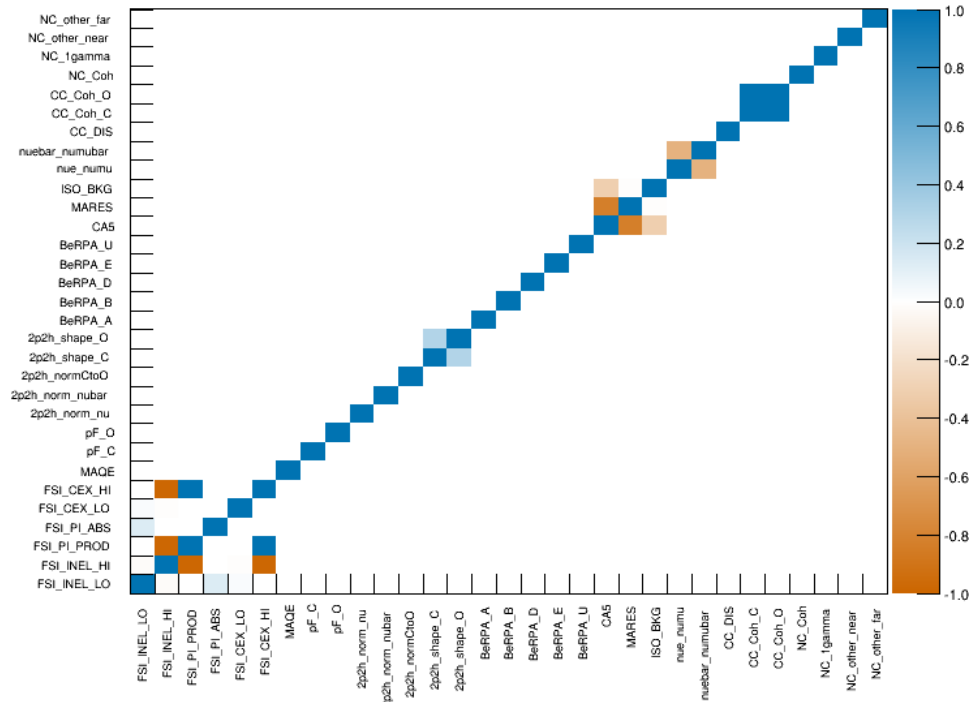
There are a total of 31 cross section parameters in the BANFF fit, four of which are fixed. The fit parameters are listed in Table 1.4 on page 40 with the associated covariance matrix shown in Figure 1.12 on page 39. Following the definition of the flux and bin normalization parameters, cross section parameters are defined as fractional differences either in shape, scale, or normalization. If no prefit uncertainty is shown in Table 1.4 on page 40, and emphasized using **red font**, then the parameter had a flat prior assigned. A model parameter with an asterisk (*) next to it is fixed in the fit. Abbreviations used in this table are “dim.-less” for dimensionless, “norm.” for normalization, “Near” for ND280, “Far” for Super-Kamiokande, and “bkg” for background. Parameters with physical units are shown in both dimensionless and dimensional values for comparison. Prefit values are relative to the NEUT nominal value.

Prefit XSec Covariance Matrix



(a) Covariance

Prefit XSec Correlation Matrix



(b) Correlation

Figure 1.12: Cross section parameters prefit covariance and correlation matrices.

Table 1.4: Cross section model parameters in the fit. See the text for a full description.

Fit index	Topology	Model	Parameter	Prefit
562		FSI shape	Low energy INEL	0 ± 0.41
563			High energy INEL	0 ± 0.34
564			PROD	0 ± 0.41
565			ABS	0 ± 0.5
566			Low energy CEX	0 ± 0.57
567			High energy CEX	0 ± 0.28
568	CC-0 π	Llewellyn-Smith	M_A^{QE} (dim.-less)	1
			M_A^{QE} (GeV/c ²)	1.20
569		RFG	p_F^C (dim.-less)	1
			p_F^C (MeV/c)	217
570			p_F^O (dim.-less)	1
			p_F^O (MeV/c)	225
571		Nieves 2p2h	ν norm. on ¹² C	1
572			$\bar{\nu}$ norm. on ¹² C	1
573			¹² C/ ¹⁶ O norm.	1
574			¹⁶ C shape location	0
575			¹² O shape location	0
576		BeRPA nuclear model (functional)	A scale	0.59 ± 0.118
577			B scale	1.05 ± 0.21
578			D scale	1.13 ± 0.1695
579			E scale	0.88 ± 0.352
580			U scale*	1.2 ± 0.1

Fit index	Topology	Model	Parameter	Prefit
581	CC-1 π	Rein-Seghal	C_A^5	0.96 ± 0.148
582		resonant 1 π prodction	M_A^{Res} (dim.-less)	1.1263 ± 0.157
			M_A^{Res} (GeV/c ²)	1.07 ± 0.15
583			I=1/2 bkg. norm.	0.74 ± 0.307
584	Other	Event rate	CC- ν_e/ν_μ^*	1 ± 0.0282
585		at SK	CC- $\bar{\nu}_e/\bar{\nu}_\mu^*$	1 ± 0.0282
586			CC-DIS shape location	0 ± 0.4
587		Coherent pion production	CC norm. on ¹² C	1 ± 0.3
588			CC norm. on ¹⁶ O	1 ± 0.3
589			NC norm.	1 ± 0.3
590		Event rate	NC-1 γ^*	1 ± 1
591			NC Other Near	1 ± 0.3
592			NC Other Far*	1 ± 0.3

1.3 BANFF Fit Parameterization Summary

This chapter has described all the fit bins and systematic parameters that go into the BANFF fit. For the fit bins, they are used in the LLR term to model the best possible fit between data and MC without any constraints. However, since there are known systematic uncertainties in the flux, detector inefficiencies, and cross sections, we have described their parameterizations to force the fit work within those constraints. The flux model is constrained by T2K primary and secondary beamline data while the cross sections are constrained by external data. Finally, the detector systematics are determined via an ensemble of toy experiments based on well established control samples in the ND280 detector.

The next chapter describe the set of validation studies used to examine how the BANFF fit performs.

Bibliography

- [1] K. Abe et al. Measurement of Coherent $\pi(+)$ Production in Low Energy Neutrino-Carbon Scattering. *Phys. Rev. Lett.*, 117(19), NOV 4 2016. 36
- [2] K. Abe et al. Measurement of neutrino and antineutrino oscillations by the T2K experiment including a new additional sample of ν_e interactions at the far detector. *Phys. Rev. D*, 96(9), NOV 21 2017. 6, 13, 14
- [3] K. Abe et al. First measurement of the ν_μ charged-current cross section on a water target without pions in the final state. *Phys. Rev. D*, 97:012001, January 2018. 13, 15
- [4] K. Abe et al. Search for CP Violation in Neutrino and Antineutrino Oscillations by the T2K Experiment with 2.2×10^{21} Protons on Target. *Phys. Rev. Lett.*, 121:171802, October 2018. 33
- [5] N. Abgrall et al. Measurements of π^\pm , K^\pm , K_S^0 , Λ and proton production in proton-carbon interactions at 31 GeV/c with the NA61/SHINE spectrometer at the CERN SPS. *Eur. Phys. J. C*, 76:84, 2016. 5
- [6] O. Benhar et al. Spectral function of finite nuclei and scattering of GeV electrons. *Nucl. Phys.*, A579:193–517, 1994. 34
- [7] Ch. Berger and L. M. Seghal. Lepton mass effects in single pion production by neutrinos. *Phys. Rev. D*, 76:113004, December 2007. 36, 37

-
-
- [8] S. Bienstock et al. Constraining the Flux and Cross Section Models with Data from the ND280 Detector using FGD1 and FGD2 for the 2017 Joint Oscillation Analysis, 2017. T2K-TN-324. 5
- [9] R. Bradford et al. A new parameterization of the nucleon elastic form factors. *Nucl. Phys.*, B159(127), 2006. 34
- [10] T. Campbell et al. The ANuMu/NuMu Cross Sections Ratio With the P0D+TPC Samples, 2017. 16
- [11] L. H. Chan et al. Nucleon Form Factors and Their Interpretation. *Phys. Rev.*, 141:1298–1307, January 1966. 34
- [12] G. Co'. Random phase approximation and neutrino-nucleus cross sections. *Acta Phys. Polon.*, B37:2235–2242, 2006. 34
- [13] R. T. Farouki. The Bernstein polynomial basis: A centennial retrospective. *Computer Aided Geometric Design*, 29(6):379–419, 2012. 35
- [14] T. Golan et al. Final State Interactions Effects in Neutrino-Nucleus Interactions. *Phys. Rev. C*, 86:015505, 2012. 37
- [15] K. M. Graczyk et al. C_A^5 axial form factor from bubble chamber experiments. *Phys. Rev.*, D80:093001, 2009. 36
- [16] K. M. Graczyk et al. Electroweak form factors of the $\Delta(1232)$ resonance. *Phys. Rev. D*, 90:093001, November 2014. 36
- [17] K. M. Graczyk and J. T. Sobczyk. Form factors in the quark resonance model. *Phys. Rev. D*, 77:053001, March 2008. 36
- [18] Krzysztof M. Graczyk and Jan T. Sobczyk. Lepton mass effects in weak charged current single pion production. *Phys. Rev. D*, 77:053003, March 2008. 36

-
-
- [19] T. Hastie et al. *The Elements of Statistical Learning: Data Mining, Inference, and Prediction*. Springer Series in Statistics. Springer New York, New York, NY, 2009. 2, 32
- [20] T. Kitagaki et al. Charged-current exclusive pion production in neutrino-deuteron interactions. *Phys. Rev. D*, 34:2554–2565, November 1986. 36
- [21] C. H. Llewellyn Smith. Neutrino Reactions at Accelerator Energies. *Phys. Rept.*, 3:261–379, 1972. 34
- [22] M. Martini et al. A Unified approach for nucleon knock-out, coherent and incoherent pion production in neutrino interactions with nuclei. *Phys. Rev.*, C80:065501, 2009. 34
- [23] J. Nieves et al. Inclusive Charged-Current Neutrino-Nucleus Reactions. *Phys. Rev.*, C83:045501, 2011. 34, 35
- [24] Kajetan Niewczas and Jan T. Sobczyk. Search for nucleon-nucleon correlations in neutrino-argon scattering. *Phys. Rev.*, C93(3):035502, 2016. 34
- [25] G. M. Radecky et al. Study of single-pion production by weak charged currents in low-energy νd interactions. *Phys. Rev. D*, 25:1161–1173, March 1982. 36
- [26] Dieter Rein and Lalit M Sehgal. Neutrino-excitation of baryon resonances and single pion production. *Ann. Phys.*, 133(1):79–153, 1981. 36
- [27] Dieter Rein and Lalit M. Sehgal. Coherent π^0 production in neutrino reactions. *Nucl. Phys. B*, 223(1):29–44, 1983. 36
- [28] G. Rowe et al. Energy-dependent phase shift analysis of pion-nucleon scattering below 400 MeV. *Phys. Rev. C*, 18:584–589, July 1978. 37
- [29] L.L. Salcedo et al. Computer simulation of inclusive pion nuclear reactions. *Nucl. Phys. A*, 484(3):557–592, 1988. 37

-
-
- [30] R.A. Smith and E.J. Moniz. Neutrino reactions on nuclear targets. *Nucl. Phys. B*, 43:605–622, 1972. 34
- [31] W. Toki. Update of P0D Inspection. Private communication, June 2016. 15
- [32] Carl Vincent Clarence Wret. *Minimising Systematic Uncertainties in the T2K Experiment Using Near-Detector and External Data*. PhD thesis, Imperial College London, 2019. 5, 13, 18, 34, 37
- [33] T. Yuan et al. Double Differential Measurement of the Flux Averaged ν_μ CC0Pi Cross Section on Water, August 2016. T2K-TN-258 v4.6.1. 24